JTTEE5 22:83–89
DOI: 10.1007/s11666-012-9838-y
1059-9630/$19.00 © ASM International

Peer Reviewed

Process Conditions and Microstructures of Ceramic Coatings by Gas Phase Deposition Based on Plasma Spraying

G. Mauer, A. Hospach, N. Zotov, and R. Vaßen

(Submitted June 19, 2012; in revised form September 20, 2012)

Plasma spraying at very low pressure (50-200 Pa) is significantly different from atmospheric plasma conditions (APS). By applying powder feedstock, it is possible to fragment the particles into very small clusters or even to evaporate the material. As a consequence, the deposition mechanisms and the resulting coating microstructures could be quite different compared to conventional APS liquid splat deposition. Thin and dense ceramic coatings as well as columnar-structured strain-tolerant coatings with low thermal conductivity can be achieved offering new possibilities for application in energy systems. To exploit the potential of such a gas phase deposition from plasma spray-based processes, the deposition mechanisms and their dependency on process conditions must be better understood. Thus, plasma conditions were investigated by optical emission spectroscopy. Coating experiments were performed, partially at extreme conditions. Based on the observed microstructures, a phenomenological model is developed to identify basic growth mechanisms.

Keywords activation energy, gas phase deposition, microstructure, plasma spray-PVD, structure zone model

1. Introduction

The very low pressure plasma spray (VLPPS) process has been developed with the aim of depositing uniform and thin coatings with large area coverage based on plasma spraying. At typical pressures of 50-200 Pa, the characteristics of the plasma jet change compared to conventional low pressure plasma spraying processes (LPPS, formerly often called vacuum plasma spraying, VPS) operating at 5-20 kPa. By VLPPS, quite thin and dense ceramic coatings can be obtained for special applications like solid oxide fuel cells (Ref 1), gas separation membranes (Ref 2), and wear protection (Ref 3).

The combination of VLPPS with enhanced electrical input power has led to the development of the plasma spray-PVD process [PS-PVD (Ref 4), initially called LPPS-TF process, TF = thin film]. At electrical currents up to 3000 A and plasma gas flow up to 200 slpm, an input power level of 180 kW could be achieved. The plasma plume expands to a length of more than 1.5 m and 200-400 mm in diameter. At appropriate parameters, it is even possible to evaporate the powder feedstock material achieving advanced microstructures and non-line of sight deposition, e.g., for thermal barrier coatings (Ref 5).

To exploit the potential of such gas-phase deposition using plasma spray-based processes, the deposition mechanisms and their dependency on process conditions must be better understood. The PS-PVD process can be pictured as occurring in three steps each with special characteristics due to the low pressure and the high power: feedstock processing in the plasma torch (1), plasma jet formation and material transport (2), deposition and coating growth (3). These sub-processes were used to structure the work described in this article.

2. Experimental Procedures

Experiments were carried out on a Sulzer Metco Multicoat System (Sulzer Metco, Wohlen, Switzerland). It resulted from a comprehensive reconstruction of an existing conventional LPPS system. In particular, it was equipped with an additional vacuum pumping unit, a large vacuum blower to provide sufficient pumping capacity at low pressures, enlarged cooling capacity, additional power sources, a new torch transfer system and new control units. In addition to a modified single cathode O3CP gun, which

This article is an invited paper selected from presentations at the 2012 International Thermal Spray Conference and has been expanded from the original presentation. It is simultaneously published in *Thermal Spray 2012: Proceedings of the International Thermal Spray Conference, Air, Land, Water, and the Human Body: Thermal Spray Science and Applications,* Houston, Texas, USA, May 21-24, 2012, Basil R. Marple, Arvind Agarwal, Laura Filofteia-Toma, Margaret M. Hyland, Yuk-Chiu Lau, Chang-Jiu Li, Rogerio S. Lima, and André McDonald, Ed., ASM International, Materials Park, OH, 2012.

G. Mauer, A. Hospach, N. Zotov, and **R. Vaßen**, Forschungszentrum Jülich, Institut für Energie- und Klimaforschung (IEK-1), Jülich, Germany. Contact e-mail: g.mauer@fz-juelich.de.

Table 1 Plasma spray parameters

Plasma gas	Ar 35 slpm He 60 slpm
Current	2600 A
Net power	60 kW
Pressure	200 Pa
Powder feed rate	1-20 g/min (varied)
Carrier gas	2 × 12 slpm Ar
Spray distance	300-1400 mm (varied)

slpm, Standard liters per minute

was used in this work, also the F4-VB torch as well as the three-cathode TriplexPro torch can be operated.

The two powder injectors were located in the cylindrical section of the O3CP nozzle (D 12.5 mm) close to the divergent part. For most of the experiments an agglomerated 7-8 wt.% Yttria partially stabilized zirconia powder (YSZ, Sulzer Metco M6700) was used. The grain sizes measured by laser diffraction were $d_{10} = 2$ μm, $d_{50} = 8$ μm, and $d_{90} = 18$ μm. Some additional samples were sprayed with a fused and crushed titania powder (TiO_2, HC Starck 782.008) with characteristic particle sizes of $d_{10} = 8$ μm, $d_{50} = 13$ μm, and $d_{90} = 19$ μm. For PS-PVD operations, the powder grain sizes should be preferably small. In contrast to the YSZ feedstock, the TiO_2 powder was not optimized for PS-PVD applications. Initially, the substrates were polished stainless steel, however, for high substrate temperatures >1200 °C, polished graphite or tungsten were used. The substrates were preheated by the plasma jet immediately before coating. Table 1 shows the appropriate plasma spray parameters. Mostly, there was no sample movement, in three cases the samples rotated at 48 min^{-1}.

The spectrometer used for plasma characterization was an HR2000 (Ocean Optics, Dunedin, FL, USA) scanning a wavelength range of 360-795 nm. The plasma radiation was collected through a borosilicate glass window and an achromatic lens, transferred by an optical fiber to the 25 μm entrance slit. The groove density of the grating was 600 mm^{-1}. Wavelength calibration was carried out with a spectral Hg lamp.

3. Results and Discussion

3.1 Feedstock Processing in the Plasma Torch

The O3CP torch was equipped with a two-fold internal powder injection. The feedstock agglomerates are fragmented into sub-micron primary particles and heated already inside the nozzle where the plasma gas density is still high before exiting. This results in the formation of molten droplets and vapor with atomic species. The reason for the high density here is that the plasma jet is significantly supersonic. This means that the plasma gas can exit the nozzle at a pressure which is different from the chamber pressure. As the flow is faster than the pressure waves traveling in the fluid at the local speed of sound, no information on the chamber pressure is carried inside the nozzle (Ref 6).

In the experiments, the development of clusters was also observed showing neither atomic nor liquid-like behavior at deposition. Such clusters may be the product of an incomplete evaporation or nucleation and growth. Similar clusters were already produced to obtain nanostructured coatings by injecting vapor phase reactants into a plasma and rapidly quenching in a supersonic nozzle (Ref 7).

YSZ particles which were collected from the PS-PVD chamber walls showed particle sizes between 5 and 20 nm. This is significantly smaller than the YSZ feedstock primary particles which were between 70 and 130 nm. Furthermore, the XRD patterns differ significantly. They indicate monoclinic zirconia and cubic yttria for the feedstock in contrast to half tetragonal and half monoclinic YSZ for the collected particles. Thus, the collected particles can be regarded to be clusters as discussed. They play an important role in the formation of either columnar or dense coating microstructures; see below. Mixed mode deposition of clusters and liquid splats was also observed depending on the process conditions.

In this study, a helium-argon mixture was used as plasma gas. Helium has a distinctly higher ionization temperature and the associated drop of viscosity takes place at much higher temperatures compared to argon (Ref 8). This leads to an increased momentum transfer to the particles. As helium and argon are both monatomic gases, they have similar molar enthalpy characteristics.

3.2 Plasma Jet Formation and Material Transport

As the chamber pressure is significantly below the nozzle exit pressure, the jet is under-expanded. The temperature and velocity distributions in the plasma jet are at higher level and more uniform compared to conventional spray processes (Ref 6). One reason is the laminar flow of the plasma: Reynolds numbers are typically very small. Therefore, the interaction of the plasma jet with the surrounding atmosphere is weak so that it is less cooled or decelerated. The homogenous energy distribution in the plasma plume allows also coating of thin substrates which are sensitive to thermal deformation.

Based on spectroscopically measured emissions, plasma temperatures can be determined by the atomic Boltzmann plot method, which is described elsewhere (Ref 9). 32 readily identifiable Ar I atomic spectral lines were selected between 516.2285 and 763.5106 nm to draw the plots. They show linear developments and the coefficients of determination for the regression lines are always $r^2 > 0.88$. At PS-PVD, the collision frequency is reduced and accordingly the mean free path in the plasma jet is increased. Local thermal equilibrium (LTE) may cease to be valid. Therefore, the obtained temperatures represent the excitation temperatures which are regarded to be equivalent to the electron temperatures.

Figure 1 shows the axial development of plasma excitation temperatures for the conditions mentioned above. The temperature decreases continuously in the downstream direction dropping below 10,000 K at 435 mm axial distance from the torch. At spray distances of >1000 mm,

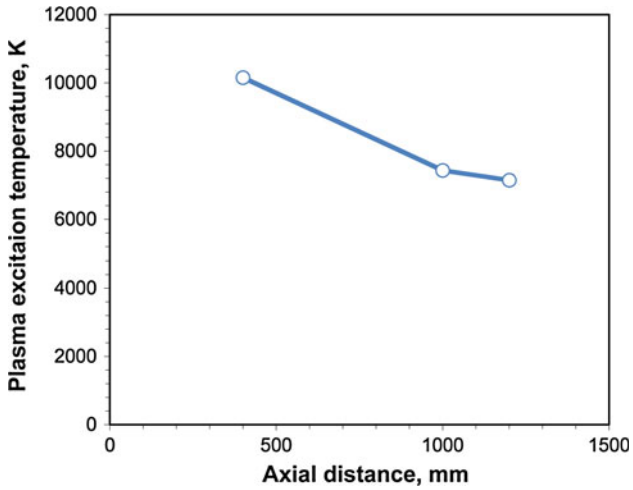

Fig. 1 Axial dependence of plasma excitation temperatures determined by spectroscopic measurements and Boltzmann plot evaluation

the values approach toward 7000 K. Such values appear high. However, the temperatures of the heavy species (atoms and ions) are supposed to be lower as LTE is likely not fulfilled. Due to the low density (Nusselt numbers are smaller compared to atmospheric pressure) particle heating in the plume is reduced. Thus, even the formation of re-solidified particles is observed. They can be incorporated in the coating. Re-solidified particles are found in the whole process chamber so that circulation with the gas flow toward the exhaustion must be assumed.

3.3 Deposition and Coating Growth

Primarily, the coating microstructure is determined by the nature of the particles arriving on the substrate. The incorporation of solid particles has already been discussed above. Liquid droplets form splats piling up to build the coating. This is the general deposition mechanism for conventional plasma spraying. At PS-PVD conditions, the deposits are formed predominantly from clusters and/or vaporized atomic species. (1) Shadowing, (2) adsorption, nucleation, and growth, (3) as well as bulk recrystallization are the basic mechanisms characterizing the coating growth.

3.3.1 Shadowing. In the case of cluster deposition, shadowing mainly occurs. This is the interaction between the roughness of the growing surface and the angular directions of the arriving particles. After sticking, the clusters are hardly mobile so that the surface roughness cannot be smoothed. Thus, the shadowing intensifies as the coating grows. The consequence is a microstructure consisting of tapered columns with domed tops and separated by voids. Figure 2 gives the examples of a typical fracture surface and a coating surface. Microstructures like this show large specific surface areas up to 10 m^2/g (measured by BET). Average porosities are between 25 and 30% (determined by digital image analysis). The formation of similar columnar structures by shadowing is also observed at suspension plasma spraying (SPS) due to

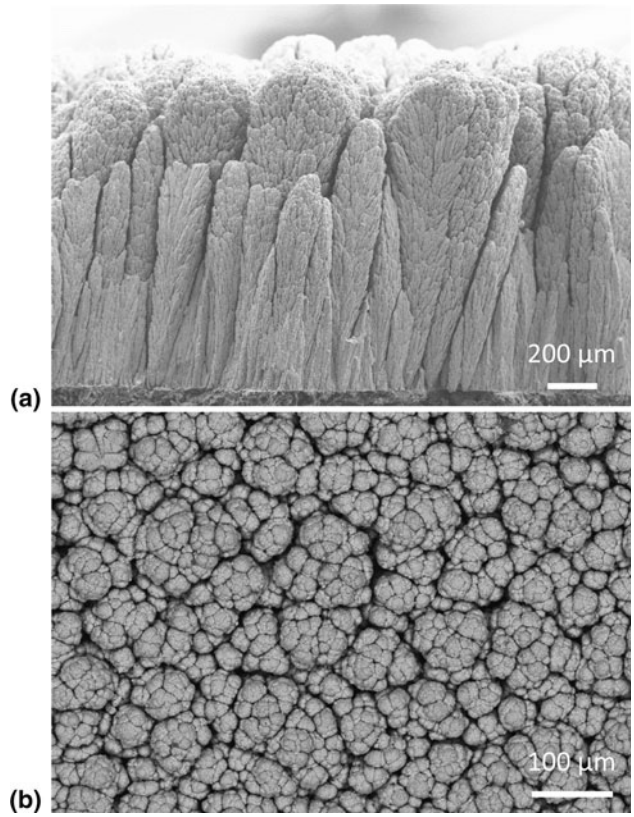

Fig. 2 Typical fracture surface (a secondary electron image) and coating surface (b backscattered electron image) of columnar YSZ structures generated by shadowing (20 g/min, 300 mm)

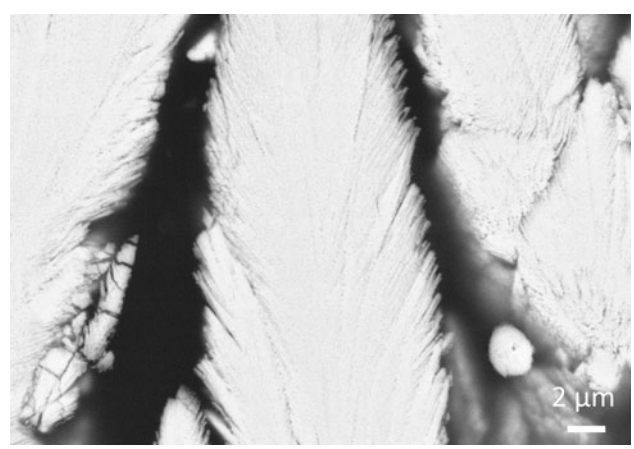

Fig. 3 Typical cross section (backscattered electron image) of columnar YSZ structures generated by shadowing (20 g/min, 1000 mm)

the size relation of deposited particles and surface roughness as well as due to the tangential components of the trajectories (Ref 10, 11). However, it has to be noted that in contrast to PS-PVD merely liquid splats are deposited by SPS.

The internal structures of the columns look feather-like consisting of fine fibers. Figure 3 shows the cross section of

an example. It is obvious that newly deposited clusters preferentially stick on the tips of these fibers. Here, shadowing occurs again, however, on a smaller scale. XRD gives no indication of any preferential growth. This supports the assumption that polycrystalline clusters are deposited and condensation from the vapor phase is present less. This is supported by the XRD patterns of such coatings which are quite similar to those of the nano-sized cluster particles which were collected from the walls of the process chamber as shown above.

As already mentioned, the angular directions of the arriving particles affect the occurrence of shadowing. This means that the plasma flow conditions close to the sample play an important role. Columnar structures are mainly observed in the center of the plasma jet where stagnation of the plasma gas flow takes place and a boundary layer is attached to the coating surface. As the tangential flow velocity decreases within such boundary layer, the direction of impingement should vary close around the surface normal. However, distant from the jet axis the flow could separate from the surface (particularly if it is curved and the velocity is high) so that vortex generation and reverse flow could occur. Such effects may overcome shadowing. This is supposed to be the reason for the smooth and dense cluster deposition observed here. Figure 4 gives an example showing such kind of dense microstructures. As they were deposited at short spray distance of 300 mm, the contrast to columnar structures formed in the jet center is very pronounced.

3.3.2 Adsorption, Nucleation, and Growth. In the case of vapor phase deposition, atomic species are adsorbed and initial nuclei are formed on the substrate surface. Their shape depends on the relation of adatom adsorption energies on the substrate, on the deposited coating, and among the adatoms themselves. So the coating may grow either in layers or more island-like (Ref 12). The mode of further growth is determined, in particular, by surface diffusion which can be quantified in terms of activation energy and impingement rate (see below). The adatoms exchange energy with the surface lattice and other adsorbed species until they are trapped at low-energy sites. By such a film recrystallization, differences in the crystal face condensation and lattice absorption probabilities can be equalized easily. Thus, the growth of the crystallite faces is balanced so that compact columnar coatings develop with faceted surfaces. Figure 5 gives a typical example.

Shadowing as described above and surface diffusion may occur at the same time as there is a certain transition region where both mechanisms overlap. Here, the columns show still coarse and tapered shapes, but the voids between the columns begin to fill and the column tips become faceted as surface recrystallization begins. Figure 6 gives such an example. XRD yields clear indication of preferential growth along the (0 0 2)/(1 1 0) and the (0 0 4)/(2 2 0) directions.

3.3.3 Bulk Recrystallization. At sufficient high temperatures, volume diffusion starts. Equiaxed grains are formed by bulk recrystallization. The coating surfaces show smooth, polyhedral structures. For high-melting coating materials, the required temperatures exceed the thermal load capacity of common substrate materials. Hence, graphite and tungsten had to be used to investigate some samples in this high temperature region.

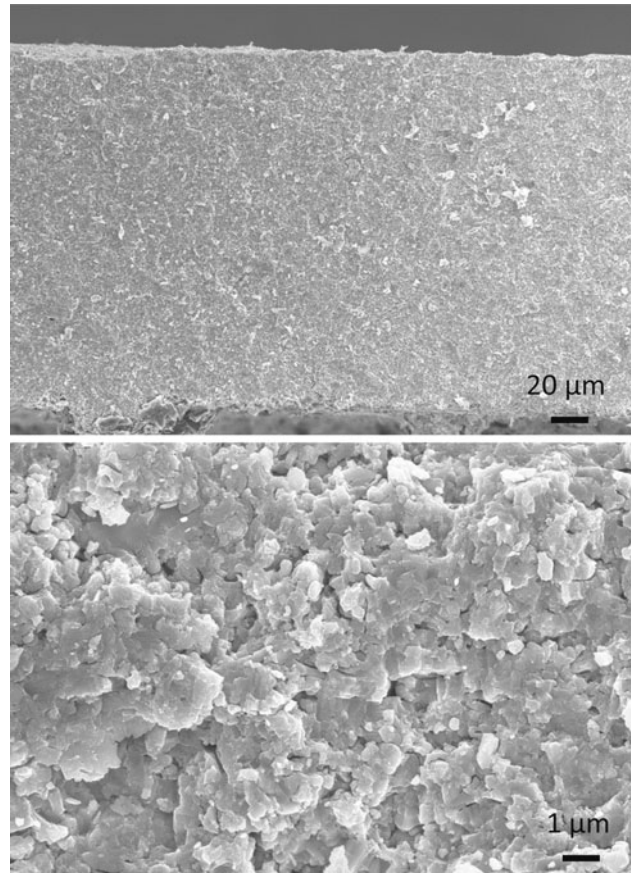

Fig. 4 Fracture surfaces (secondary electron images) of dense YSZ structures by cluster deposition (20 g/min, 300 mm, 40 mm offset from jet center)

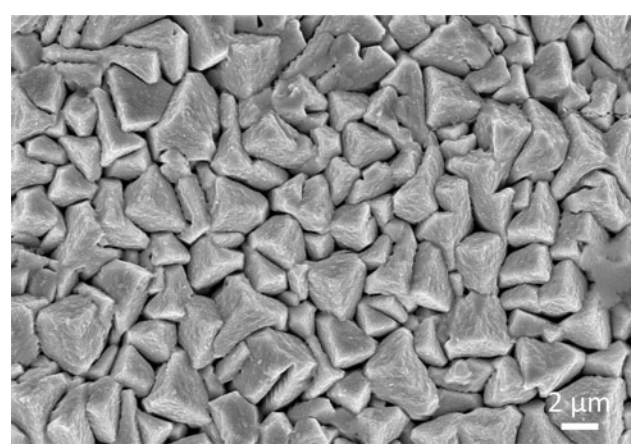

Fig. 5 Typical coating surface of columnar YSZ structures generated by surface diffusion (2 g/min, 300 mm; secondary electron image)

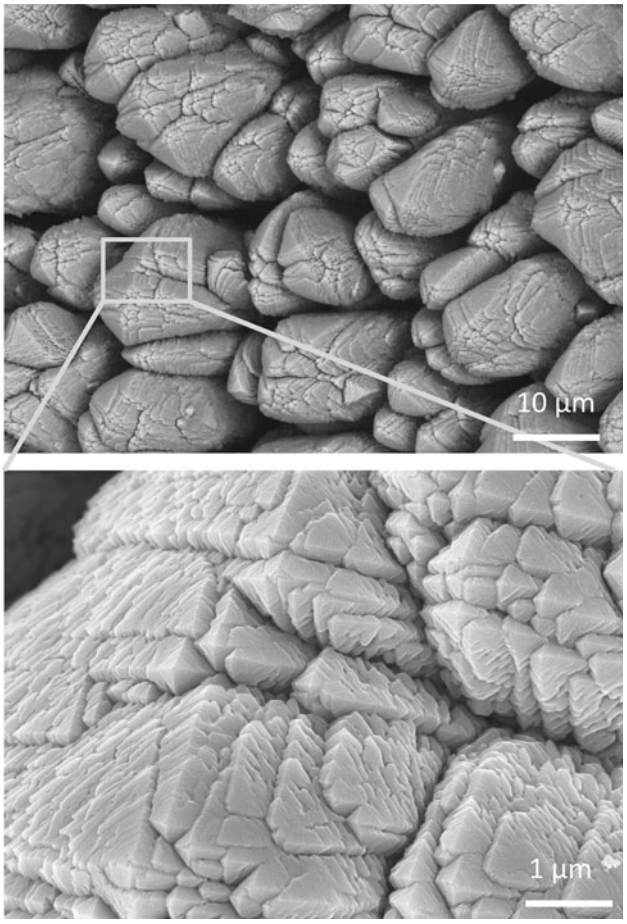

Fig. 6 Typical coating surface of columnar YSZ structures generated in the transitional region of shadowing and surface diffusion (2 g/min, 800 mm; backscattered electron image)

3.3.4 Structure Zone Model (SZM). For many materials, the activation energies of surface and bulk diffusion can be related to the melting point T_m. Thus, these mechanisms can be expected to dominate over different ranges of the homologous temperature of the substrate surface T_s/T_m. This is the basis of SZMs (Ref 13). The Movchan-Demchishin SZM (Ref 14) was developed based on thick coatings (0.3-2 mm) of Ti, Ni, W, Al_2O_3, and ZrO_2 made by electron beam evaporation. Three zones were defined, each with its own structure and properties which correspond well with the characteristics of PS-PVD coatings formed by shadowing, surface, and bulk diffusion as described above. The transition temperatures for oxides were given by $T_s/T_m = 0.22\text{-}0.26$ between zones 1 and 2 as well as $T_s/T_m = 0.45\text{-}0.5$ between zones 2 and 3.

Thornton (Ref 15, 16) investigated 25-250 µm thick magnetron sputtered coatings of Ti, Cr, Fe, Cu, Mo, and Al alloys and introduced a transitional zone T between zones 1 and 2. The characteristics of the zones 1, 2, and 3 are in good agreement with the Movchan-Demchishin SZM. Moreover, a second axis was added to account for the sputtering gas pressure. Figure 7 shows this SZM. It is suggested that reduced adatom mobility is involved by

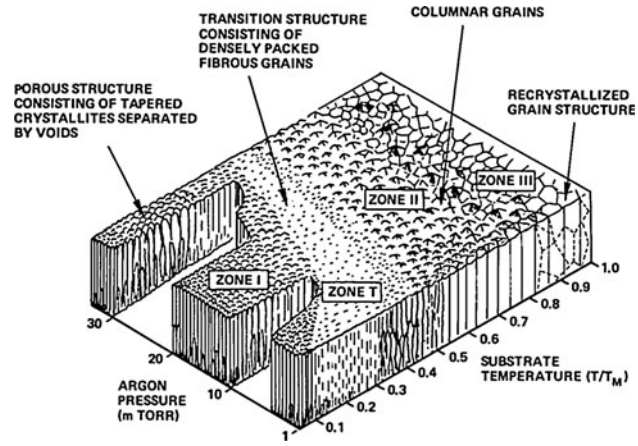

Fig. 7 Structure zone model for magnetron sputtered coatings proposed by Thornton (Ref 15, 16)

increased inert gas pressure. Consequently, the transitional zone T is shifted to higher temperatures at increasing pressure. Messier et al. (Ref 17) revised the Thornton SZM by replacing the parameter of the sputtering gas pressure by the substrate bias voltage to consider the effect on adatom mobility. Musil et al. (Ref 18) suggested replacing global parameters, such as pressure or bias voltage, by an energy parameter which combines ion energy with the fluxes of ions and condensing atoms.

The considerations to develop SZMs can be transferred to PS-PVD. As described above, the characteristics of PS-PVD coatings correspond well to zones 1, 2, and 3 identified by Movchan-Demchishin and Thornton. Moreover, attributes between zones 1 and 2 similar to the characteristics of zone T are present also in PS-PVD coatings. It is obvious that the substrate temperature is one significant parameter also for the PS-PVD model as surface and bulk diffusion determine the formation of the zones. For PS-PVD, the second model parameter is the impingement rate as the free path for adatom surface diffusion is directly affected. The condition for coating growth without nucleation is (Ref 12)

$$\dot{N} \leq N_0^2 D, \qquad \text{(Eq 1)}$$

where $\dot{N}$ represents the area-specific impingement rate (particles/m^2·s), N_0 the number of suitable lattice sites (1/m^2), and D the diffusion coefficient (m^2/s).

In this study, PS-PVD manufactured coatings were investigated regarding substrate temperatures and deposition rates in relation to the characteristic features of the coating microstructure. The homologous substrate temperatures T_s/T_m were calculated as well as the area-specific impingement rates $\dot{n}$ (mol/m^2 · s) according to

$$\dot{n} = \frac{\dot{N}}{N_A} = \dot{d}\frac{\rho}{M}, \qquad \text{(Eq 2)}$$

where N_A represents the Avogadro number (1/mol), $\dot{d}$ the coating deposition rate (m/s) and M/ρ the molar volume (m^3/mol).

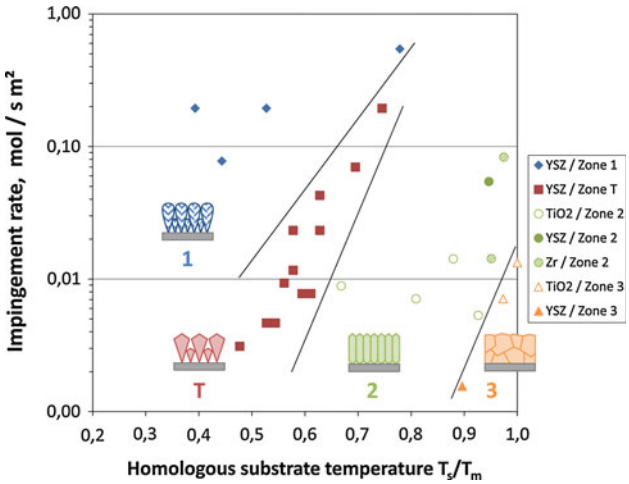

Fig. 8 PS-PVD structure zone model

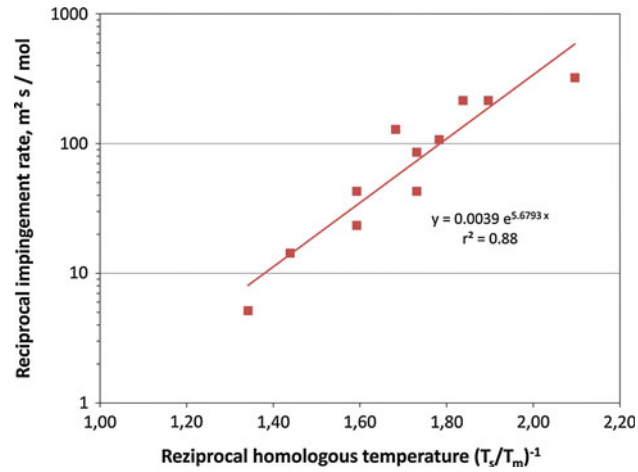

Fig. 9 Logarithm of the impingement rate versus the reciprocal temperature for determination of the activation energy

It must be noted that the original design of experiments was not intended to build up a SZM. Hence, there are some parameter regions being covered only poorly. Figure 8 shows the PS-PVD SZM as far as the zones could be identified. The nomenclature of the zones corresponds to the Thornton SZM. By calculating the homologous temperatures and mole rates, experiments with different materials could be considered in the same diagram.

The consistence with the Thornton SZM is evident. In particular, the oblique and narrowing shape of zone T is similar. The transition line between zones 2 and 3 should be independent on the impingement rate and thus proceed vertically as bulk diffusion is not affected by reduced surface mobility. This is more obvious in the Thornton SZM.

3.3.5 Activation Energy for Surface Diffusion. As mentioned above, surface diffusion can be quantified in terms of activation energy and impingement rate. Hence, for nucleation and growth rate being equal, Eq 1 can be written as

$$\dot{n} = \frac{N_0^2 D_0}{N_A} e^{\frac{-Q}{RT}}, \qquad \text{(Eq 3)}$$

where D_0 represents the pre-exponential factor (m^2/s), Q the activation energy (J/mol), and R the universal gas constant (J/mol · K). Taking the logarithm of the reciprocal terms in Eq 3 yields

$$\ln\left(\frac{1}{\dot{n}}\right) = \ln\left(\frac{N_A}{N_0^2 D_0}\right) + \frac{Q}{RT}. \qquad \text{(Eq 4)}$$

This means that by logarithmical plotting the impingement rate versus the reciprocal temperature and calculating an exponential regression function for the data points of zone T which represent microstructures with first indications of surface diffusion, the activation energy can be determined from its slope.

Figure 9 shows such plot (YSZ only). As the amount of surface diffusion for each data point is not well defined and their distribution is not systematic this can be only an initial approach. The calculation of the activation energy yields 141 kJ/mol. Reference values for surface diffusion are scarce and inconsistent, in particular, for tetragonal YSZ. Activation energies for fully developed cation surface diffusion are reported between 314 and 531 kJ/mol (Ref 19). At PS-PVD conditions, surface diffusion could be facilitated as the surfaces can be regarded as very clean; furthermore, plasma activation could have an effect so that smaller thermal activation energies are needed.

4. Summary and Conclusion

By PS-PVD, it is possible to evaporate the powder feedstock at appropriate parameters providing advanced microstructures and non-line of sight deposition. To ensure evaporation of the feedstock, the conditions inside the nozzle in proximity to the location of injection are crucial. High-power density and accommodated feedstock characteristics are required. Besides evaporation, the formation of nano-sized clusters is observed. Having exited the nozzle, further particle heating is reduced compared to atmospheric pressure due to the low density (Nusselt numbers are smaller).

For coating growth, a SZM was developed following the work of Thornton. The analysis reveals different growth mechanisms like shadowing, surface, and bulk diffusion. Vapor deposition of compact columnar structures is only possible if the surface mobility of the adatoms is sufficient. This is obtained by high substrate temperatures and low deposition rates. The activation energy for surface diffusion was initially estimated by 141 kJ/mol for YSZ which is relatively low.

References

1. C. Verdy, C. Zhang, D. Sokolov, H. Liao, D. Klein, and C. Coddet, Gas-tight Coatings Produced by Very Low Pressure Plasma Spraying, *Thermal Spray 2008: Thermal Spray Crossing Borders*, on CD-ROM, E. Lugscheider, Ed., June 02-04, 2008

(Maastricht, The Netherlands), Verlag für Schweißen und verwandte Verfahren, 2008, p 398-402
2. G. Mauer, R. Vaßen, and D. Stöver, Thin and Dense Ceramic Coatings by Plasma Spraying at Very Low Pressure, *J. Therm. Spray Technol.*, 2010, **19**(1-2), p 495-501
3. L. Zhu, N. Zhang, B. Zhang, F. Sun, R. Bolot, M.-P. Planche, H. Liao, and C. Coddet, Very Low Pressure Plasma Sprayed Alumina and Yttria-Stabilized Zirconia Thin Dense Coatings Using a Modified Transferred Arc Plasma Torch, *Appl. Surf. Sci.*, 2011, **258**(4), p 1422-1428
4. K. von Niessen and M. Gindrat, Plasma Spray-PVD: A New Thermal Spray Process to Deposit Out of the Vapor Phase, *J. Therm. Spray Technol.*, 2011, **20**(4), p 736-743
5. K. von Niessen, M. Gindrat, and A. Refke, Vapor Phase Deposition Using Plasma Spray-PVD, *Therm. Spray Technol.*, 2010, **19**(1-2), p 502-509
6. B. Jodoin, M. Gindrat, J.-L. Dorier, C. Hollenstein, M. Loch, and G. Barbezat, Modeling and Diagnostics of a Supersonic DC Plasma Jet Expanding at Low Pressure, *International Thermal Spray Conference*, E. Lugscheider, C.C. Berndt, Ed., March 04-06, 2002 (Essen, Germany), Verlag für Schweißen und verwandte Verfahren DVS-Verlag, 2002, p 716-720
7. J. Hafiz, R. Mukherjee, X. Wang, P.H. McMurry, J.V.R. Heberlein, and S.L. Girshick, Hypersonic Plasma Particle Deposition-A Hybrid between Plasma Spraying and Vapor Deposition, *J. Therm. Spray Technol.*, 2006, **15**(4), p 822-826
8. J. Aubreton, M.F. Elchinger, V. Rat, and P. Fauchais, Two-Temperature Transport Coefficients in Argon-Helium Thermal Plasmas, *J. Phys. D*, 2004, **37**, p 34-41
9. G. Mauer, R. Vaßen, and D. Stöver, Plasma and Particle Temperature Measurements in Thermal Spray: Approaches and Applications, *J. Therm. Spray Technol.*, 2011, **20**(3), p 391-406
10. H. Kaßner, R. Siegert, D. Hathiramani, R. Vaßen, and D. Stöver, Application of Suspension Plasma Spraying (SPS) for Manufacture of Ceramic Coatings, *J. Therm. Spray Technol.*, 2008, **17**(1), p 115-123
11. K. VanEvery, M.J.M. Krane, R.W. Trice, H. Wang, W. Porter, M. Besser, D. Sordelet, J. Ilavsky, and J. Almer, Column Formation in Suspension Plasma-Sprayed Coatings and Resultant Thermal Properties, *J. Therm. Spray Technol.*, 2011, **20**(4), p 817-828
12. J.A. Venables, G.D.T. Spiller, and M. Hanbücken, Nucleation and Growth of Thin Films, *Rep. Prog. Phys.*, 1984, **47**, p 399-459
13. J.A. Thornton, High Rate Thick Film Growth, *Ann. Rev. Mater. Sci.*, 1977, **7**, p 239-260
14. B.A. Movchan and A.V. Demchishin, Study of the Structure and Properties of Thick Vacuum Condensates of Nickel, Titanium, Tungsten, Aluminum Oxide and Zirconium Dioxide, *Phys. Met. Metallogr.*, 1969, **28**(4), p 83-90
15. J.A. Thornton, Influence of Apparatus Geometry and Deposition Conditions on Structure and Topography of Thick Sputtered Coatings, *J. Vac. Sci. Technol.*, 1974, **11**(4), p 666-670
16. J.A. Thornton, Influence of Substrate Temperature and Deposition Rate on Structure of Thick Sputtered Cu Coatings, *J. Vac. Sci. Technol.*, 1975, **12**(4), p 830-835
17. R. Messier, A.P. Giri, and R.A. Roy, Revised Structure Zone Model for Thin Film Physical Structure, *J. Vac. Sci. Technol., A*, 1984, **2**(2), p 500-503
18. J. Musil, S. Kadlec, V. Valvoda, R. Kužel, and R. Černý, Ion-Assisted Sputtering if TiN Films, *Surf. Coat. Technol.*, 1990, **43/44**, p 259-269
19. X. Wang and A. Atkinson, Microstructure Evolution in Thin Zirconia Films: Experimental Observation and Modeling, *Acta Mater.*, 2011, **59**, p 2514-2525